Quantifying spatiotemporal chaos in Rayleigh-Bénard convection

A. Karimi and M. R. Paul

Phys. Rev. E **85**, 046201 — Published 2 April 2012

DOI: 10.1103/PhysRevE.85.046201

Quantifying Spatiotemporal Chaos in Rayleigh-Bénard Convection

A. Karimi
Department of Engineering Science and Mechanics, Virginia Polytechnic Institute and State University, Blacksburg, Virginia 24061

M. R. Paul
Department of Mechanical Engineering, Virginia Polytechnic Institute and State University, Blacksburg, Virginia 24061

Using large-scale parallel numerical simulations we explore spatiotemporal chaos in Rayleigh-Bénard convection in a cylindrical domain with experimentally relevant boundary conditions. We use the variation of the spectrum of Lyapunov exponents and the leading order Lyapunov vector with system parameters to quantify states of high-dimensional chaos in fluid convection. We explore the relationship between the time dynamics of the spectrum of Lyapunov exponents and the pattern dynamics. For chaotic dynamics we find that all of the Lyapunov exponents are positively correlated with the leading order Lyapunov exponent and we quantify the details of their response to the dynamics of defects. The leading order Lyapunov vector is used to identify topological features of the fluid patterns that contribute significantly to the chaotic dynamics. Our results show a transition from boundary dominated dynamics to bulk dominated dynamics as the system size is increased. The spectrum of Lyapunov exponents is used to compute the variation of the fractal dimension with system parameters to quantify how the underlying high-dimensional strange attractor accommodates a range of different chaotic dynamics.

PACS numbers: 05.45.Jn, 47.54.-r, 47.20.Bp, 05.45.Pq

I. INTRODUCTION

At the core of many problems of scientific interest is a spatially extended system that is driven far-from-equilibrium to yield spatiotemporal chaos (aperiodic dynamics in both space and time) [1]. Examples include the dynamics of the weather and climate [2]; fluid turbulence [3]; the intricate patterns that occur for reacting, diffusing and advecting chemicals [4]; and the transition to chaos in excitable media such as cardiac tissue [5]. It is expected for systems such as these that the dimension describing the attractor of the dynamics will be very large. As a result, the powerful ideas of chaotic time series analysis [6], as well as geometrical based approaches for estimating the dimension [7], are difficult to apply and are often ineffective.

However, with the advance and availability of sophisticated parallel algorithms and supercomputing resources these high-dimensional systems are accessible to Lyapunov exponent and Lyapunov vector based diagnostics. Using the standard approach [8] of simultaneously evolving the tangent space equations with frequent Gram-Schmidt reorthonormalizations allows one to compute the spectrum of Lyapunov exponents. With knowledge of the Lyapunov exponents the fractal dimension can be estimated using the well known Kaplan-Yorke equation [9].

A powerful aspect of this approach is that very large dimensions are now accessible with an algorithm that scales readily to parallel computing resources. Using this approach we discuss results for Rayleigh-Bénard convection which is the buoyancy driven fluid convection that occurs in a shallow fluid layer that is heated uniformly from below. Rayleigh-Bénard convection is a canonical system for the study of pattern formation in systems that are driven far-from-equilibrium [1, 10]. The study of Rayleigh-Bénard convection continues to play an important role in building our physical understanding of the complex dynamics that occur in driven spatially-extended systems.

The desire for a quantitative understanding of high-dimensional spatiotemporal chaos for experimentally accessible systems is an important challenge. In this paper we discuss results for experimentally accessible conditions with fractal dimensions as large as 50. To the best of our knowledge this represents the highest dimension dynamics that have been explored using Lyapunov based diagnostics for laboratory conditions. Knowledge of the fractal dimension can be used to provide fundamental insights into the underlying chaotic dynamics. The numerical value of the fractal dimension provides an estimate for the number of chaotic degrees of freedom that are active in the system [7]. Given the number of chaotic degrees of freedom that describe the dynamics one can construct estimates for the length scales of these degrees of freedom on average. In addition, the variation of the fractal dimension with changing system parameters allows one to probe quantitatively how the attractor accommodates different dynamics.

In the literature there are a number of new insights provided by the study of fluid convection using information gained from computing Lyapunov based diagnostics. Egolf *et al.* [11] demonstrated that Rayleigh-Bénard convection exhibited extensive chaos for large periodic domains with aspect ratios $48 \leq \Gamma \leq 64$ where $\Gamma = L/d$, L is the side length of the domain, and d is the depth of the fluid layer. In this study the system parameters were chosen to yield the spiral defect chaos state [12]. The spatiotemporal dynamics of the leading order Lya-

punov vector was studied and was found to be largest in regions where roll pinch-off events were occurring. It was suggested that the dynamics of these local defects were contributing significantly to the disorder as opposed to the visually striking spiral structures.

Scheel and Cross [13] used the leading-order Lyapunov exponent and Lyapunov vector to perform a careful study of the time-periodic and chaotic dynamics that occur in a small cylindrical convection layer with $\Gamma = 5$ (where $\Gamma = r_0/d$ and r_0 is the radius of the convection domain). They conclude that repeating local defect dynamics involving roll pinch-off events contribute significantly to the short-time Lyapunov exponent without affecting the long-time Lyapunov exponent. Interestingly, they find that the non-repeating roll pinch-off events are what contribute significantly to the long-time Lyapunov exponent. This raises several interesting questions. How does the leading order Lyapunov exponent discern between repeating and non-repeating events? How do the other Lyapunov exponents in the Lyapunov spectrum respond to these events? In this paper we will shed some further insight upon these questions.

Paul *et. al* [14] computed the spectrum of Lyapunov exponents for chaotic convection in cylindrical domains for aspect ratios $4.72 \lesssim \Gamma \leq 15$. It was determined that Rayleigh-Bénard convection was extensively chaotic for $\Gamma \gtrsim 7$. Jayaraman *et al.* [15] explored the leading-order Lyapunov exponent and Lyapunov vector for the domain chaos state that occurs for Rayleigh-Bénard convection in a rotating domain. An interesting feature of domain chaos is the presence of propagating fronts as well as localized defect structures. A careful study revealed that not all defect structures contributed equally to the leading order Lyapunov exponent, a result that is in agreement with the findings of Scheel and Cross [13] for the spiral defect chaos state.

In this paper we present a detailed study of chaotic Rayleigh-Bénard convection using diagnostics based on the spectrum of Lyapunov exponents and Lyapunov vectors for a range of experimentally relevant conditions. In Section II we describe the numerical approach used to compute the flow fields, Lyapunov exponents, and Lyapunov vectors. In Section III we discuss the dynamics of the Lyapunov exponents, the spatiotemporal features of the leading order Lyapunov vector, and the variation of the fractal dimension with system parameters. Lastly, in Section IV we present our concluding remarks.

II. APPROACH

A. Rayleigh-Bénard Convection

Rayleigh-Bénard convection is the buoyancy-driven motion that results when a thin layer of fluid is heated uniformly from below. The fluid motion is described by the Boussinesq equations,

$$\sigma^{-1}\left(\partial_t + \mathbf{u}\cdot\nabla\right)\mathbf{u} = -\nabla p + \nabla^2\mathbf{u} + RT\hat{\mathbf{z}}, \quad (1)$$

$$\left(\partial_t + \mathbf{u}\cdot\nabla\right)T = \nabla^2 T, \quad (2)$$

$$\nabla\cdot\mathbf{u} = 0, \quad (3)$$

where $\hat{\mathbf{z}}$ is a unit vector in the z-direction that opposes gravity, σ is the Prandtl number, R is the Rayleigh number, $\mathbf{u}$ is the fluid velocity, p is the pressure, and T is the temperature. The equations are nondimensionalized using the layer depth d for the length scale, the vertical diffusion time for heat d^2/α where α is the thermal diffusivity for the time scale, and the constant temperature difference between the bottom and top plates ΔT as the temperature scale.

The no-slip boundary condition is applied to all material surfaces

$$\mathbf{u} = 0 \quad (4)$$

and the lateral side-walls of the cylindrical domain are assumed to be perfectly conducting

$$T(z) = 1 - z. \quad (5)$$

The Rayleigh number,

$$R = \frac{g\beta\Delta T d^3}{\nu\alpha} \quad (6)$$

is the control parameter that is most often varied in experiment. Small values of R correspond to simple, often time-independent flows; intermediate values of R correspond to complex chaotic flows as studied here; and large values of R correspond to strongly driven turbulent flows [16]. It will be convenient to use the reduced Rayleigh number $\epsilon = (R - R_c)/R_c$ where $R_c = 1707.76$ is the critical Rayleigh number for an infinite layer of fluid. The Prandtl number,

$$\sigma = \frac{\nu}{\alpha} \quad (7)$$

is the ratio of momentum and thermal diffusivities. The magnitude of the Prandtl number is inversely related to the strength of the mean flow [17]. The mean flow is a weak but long-range flow field that originates from the Reynolds stress term and is driven by roll curvature, roll compression, and gradients in the convection amplitude [18]. The mean flow is very difficult to measure experimentally [19, 20] and has a dramatic effect upon the linear stability of the convection rolls [21, 22]. Its importance is not due to its strength, but because it is a nonlocal effect acting over large distances (many roll widths) and advects the pattern [23].

The aspect ratio of the domain Γ is a measure of the spatial extent of the system. The dynamics of the flow field depends strongly upon the aspect ratio of the fluid layer [24]. For small domains the sidewalls tend to frustrate the dynamics due to the tendency of the convection

rolls to approach a sidewall with the roll axis perpendicular to the boundary. In cylindrical domains this leads to the presence of wall foci which can penetrate several roll wavelengths into the domain. As the aspect ratio increases the influence of the sidewalls diminishes.

B. Computing the Lyapunov Exponents and Lyapunov Vectors

We compute the spectrum of Lyapunov exponents λ_k using the standard procedure described in detail in Ref. [8]. For each exponent a set of equations linearized about Eqs. (1)-(3) are evolved simultaneously to yield the dynamics of perturbations arbitrarily close to the full nonlinear system. These tangent space equations are:

$$\sigma^{-1}\left(\partial_t \delta\mathbf{u}^{(k)} + \mathbf{u}\cdot\nabla\delta\mathbf{u}^{(k)} + \delta\mathbf{u}^{(k)}\cdot\nabla\mathbf{u}\right) = -\nabla\delta p^{(k)} + \nabla^2\delta\mathbf{u}^{(k)} + R\delta T^{(k)}\hat{\mathbf{z}}, \quad (8)$$

$$\partial_t \delta T^{(k)} + \mathbf{u}\cdot\nabla\delta T^{(k)} + \delta\mathbf{u}^{(k)}\cdot\nabla T = \nabla^2\delta T^{(k)}, \quad (9)$$

$$\nabla\cdot\delta\mathbf{u}^{(k)} = 0. \quad (10)$$

which can be written as,

$$\frac{d\delta\mathbf{H}^{(k)}}{dt} = \mathbf{J}\left[\mathbf{H}(t)\right]\delta\mathbf{H}^{(k)}, \quad (11)$$

where $\mathbf{H}(t) = [\mathbf{u}, T]$ and $\delta\mathbf{H}^{(k)}(t) = \left[\delta\mathbf{u}^{(k)}(t), \delta T^{(k)}(t)\right]$. For incompressible fluid flow the pressure is implicitly determined by the requirement of the conservation of mass. As a result, the vectors $\mathbf{H}(t)$ and $\delta\mathbf{H}^{(k)}(t)$ do not include p and δp, respectively. In our notation, $\mathbf{J} = d\mathbf{F}/d\mathbf{H}$ where $\mathbf{J}$ is the Jacobian of the flow that results when rewriting Eqs. (1)-(3) as $d\mathbf{H}(t)/dt = \mathbf{F}(\mathbf{H})$. The boundary conditions for the perturbation equations are $\delta\mathbf{u}^{(k)} = \mathbf{0}$ and $\delta\mathbf{T}^{(k)} = 0$ at all material walls.

The perturbations are reorthonormalized using a Gram-Schmidt procedure after a time t_N to yield the magnitude of their growth $\|\delta\mathbf{H}^{(k)}(t_N)\|$ where the normalization is defined over the interior volume V as,

$$\|\delta\mathbf{H}^{(k)}(t)\| = \sqrt{\frac{1}{V}\int_V \left[\delta\mathbf{u}^{(k)}(t)^2 + \delta T^{(k)}(t)^2\right] dV}. \quad (12)$$

Each reorthonormalization yields a value of the instantaneous Lyapunov exponent,

$$\tilde{\lambda}_k = \frac{1}{t_N}\ln\|\delta\mathbf{H}^{(k)}(t_N)\|. \quad (13)$$

This is repeated and the average value of $\tilde{\lambda}_k$ yields the finite time Lyapunov exponent

$$\lambda_k = \frac{1}{N_t}\sum_{i=1}^{N_t}\tilde{\lambda}_k \quad (14)$$

where N_t is the number of reorthonormalizations performed. The limit $N_t \to \infty$ yields the infinite-time Lyapunov exponent.

The leading-order exponent λ_1 describes the growth of the line separating two trajectories in phase space, $\lambda_1 + \lambda_2$ describes the growth of a two-dimensional area of initial conditions, and $\sum_{i=1}^{N}\lambda_i$ describes the growth of an N-dimensional ball of initial conditions. The exact number of exponents required for the sum to vanish corresponds to the dimension of the ball of initial conditions that will neither grow nor shrink under the dynamics and is referred to as Lyapunov or fractal dimension D_λ. Given only the Lyapunov exponents, D_λ can be determined from the Kaplan-Yorke formula,

$$D_\lambda = K + \frac{S_K}{|\lambda_{K+1}|}, \quad (15)$$

where K is the largest n for which $S_n = \sum_{i=1}^{n}\lambda_i > 0$ [1, 9]. The value of D_λ is the minimum number of active degrees of freedom that contribute to the chaotic dynamics [7].

To solve the system of equations given by Eqs. (1)-(3) and Eqs. (8)-(10) we used a highly efficient, parallel spectral element code developed to solve the Boussinesq equations. This code has been used in a number of numerical explorations of Rayleigh-Bénard convection that have been discussed in the literature (c.f. [13–15, 17, 25–27]). The underlying numerical approach is discussed in Refs. [28, 29] and a discussion of its application to Rayleigh-Bénard convection can be found in Ref. [26].

In our numerical simulations, we begin from a small random perturbation on the order of 10^{-3} to the linear conduction temperature profile with zero velocity field. The initial conditions for the tangent space equations are zero perturbation velocity and a random temperature perturbation with a magnitude on the order of 10^{-5}. A typical value of the numerical time step is $\Delta t = 10^{-3}$ and we perform a Gram-Schmidt reorthonormalization every 10 time steps. Within each spectral element we have used 11^{th} order polynomials to represent the field variables.

Over the course of this work we have performed numerous tests by varying the numerical parameters used in the code to ensure the validity of our numerical results. In particular, we have performed simulations for varying time steps and spatial discretizations to ensure that our results for the Lyapunov-based diagnostics are accurate and reproducible. For a typical numerical simulation we integrate the equations for approximately 15 horizontal diffusion times to allow for initial transients to decay. We then use the numerical data from the latter half of the simulation to compute the Lyapunov diagnostics that we report here. Where possible we have included error bars in our results to reflect the variation in the quantities presented based upon our numerical results.

III. DISCUSSION

A typical chaotic flow field pattern from our numerical simulations is shown in Fig. 1. The contours of the

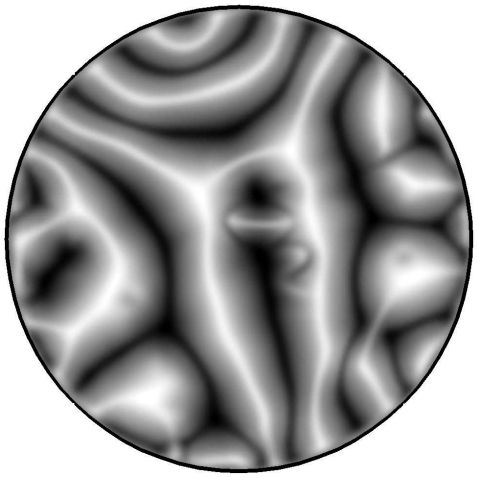

FIG. 1: A spatiotemporally chaotic flow field for $\epsilon = 4.27$, $\sigma = 1$, and $\Gamma = 10$. Contours are shown of the temperature field at a mid-plane slice where $z = 1/2$. Light regions are hot rising fluid and dark regions are cool falling fluid. This flow field image is at time $t = 610.5$.

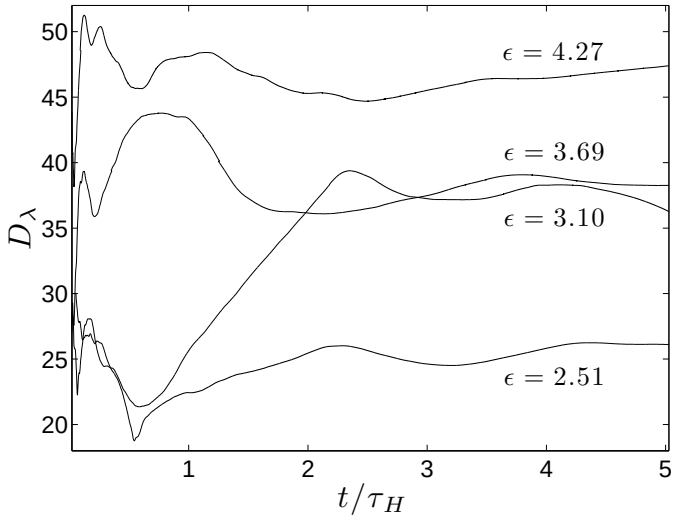

FIG. 2: The convergence of the fractal dimension D_λ in time. Results are shown for 4 different values of the reduced Rayleigh number ϵ where $\Gamma = 10$ and $\sigma = 1$. The time scale has been normalized by the horizontal diffusion time for heat, $\tau_H = \Gamma^2$. The convergence is quite slow and remains noisy over the entire range shown.

temperature field are shown at mid-depth where light regions are hot rising fluid and dark regions are cool falling fluid. The fractal dimension D_λ of this flow field is approximately 50. The convergence of D_λ in time is shown in Fig. 2 for a range of reduced Rayleigh numbers. To emphasize the slow and noisy convergence the time axis has been normalized by the nondimensional horizontal diffusion time $\tau_H = \Gamma^2$ which represents the time required for heat to diffuse from the center of the domain to the sidewall. Time scales on the order of the horizontal diffusion time for heat and longer have been shown to describe the duration required for large aspect ratio convecting systems to reach dynamics that are independent of initial transients [23].

A. The Dynamics of the Lyapunov Exponents

We are interested in understanding how the time dynamics of the Lyapunov exponents relate to the dynamics of the flow field. Only the leading order Lyapunov vector is pointing in a physically relevant direction due to the Gram-Schmidt reorthonormalizations that are used in their computation. The magnitude of the Lyapunov exponents are not affected by this and the variation of their magnitude in time provides insight into the underlying dynamics. For example, it would be useful to know if the different exponents exhibit different dynamics that could be related to features of the pattern dynamics such as roll pinch-off events, pattern rotation, and the effects of weak long-range contributions such as the mean flow.

As either R or Γ increase the patterns become very complex making it difficult to disentangle distinct features in the pattern dynamics that correspond to the variation in the magnitude of the Lyapunov exponents. In light of this, we first explore a small cylindrical domain that exhibits periodic dynamics in time. The specific parameters used are $\Gamma = 5$, $\sigma = 1$, and $\epsilon = 1.93$. Flow field images are shown in Fig. 3(a)-(b) and the variation of the Nusselt number N is shown in Fig. 3(c).

Although N is a global measure of the heat transport through the convection layer its variation with time directly corresponds with the topological features of the pattern dynamics (c.f. [25]). Figure 3(c) shows one period of the dynamics which occurs over a time of $t \approx 27$ time units. The vertical dashed lines of Fig. 3(c) indicate the times at which the flow fields in Fig. 3(a) and 3(b) are shown. The dips in $N(t)$ occur during roll pinch-off events and the positive spikes occur during dislocation annihilation events. Physically, this reflects that the heat transport through the convection layer is less efficient in the presence of the defects. The remaining smooth features of $N(t)$ correspond to climbing and gliding dynamics.

The time variation of the three largest Lyapunov exponents are shown in Fig. 4. The exponents have been normalized by the maximum value of λ_1 over this time window in order to compare them on a single plot. The normalized exponents are denoted by $\tilde{\lambda}$. As expected, the leading order Lyapunov exponent exhibits significant variations at the roll pinch-off and annihilation events. The dynamics of the second and third exponents tend to follow with some interesting variations.

For example, a closer inspection of the time dynamics near $t \approx 579$ reveals that the dynamics of λ_1 correspond precisely with the dynamical events of the pattern. However, the first peak of λ_2 is before the occurrence of the roll annihilation and anticipates this feature. In addition,

the roll pinch-off event that occurs at $t \approx 581$ results in a peak in λ_2 while both λ_1 and λ_3 exhibit dips. The dynamics of λ_3 is much more sensitive to the event that occurs near $t \approx 581$ than the event near $t \approx 579$.

In order to explore this further for chaotic dynamics we performed a number of simulations for a larger cylindrical domain with increased values of the Rayleigh number. The specific parameters we used were $\Gamma = 10$, $\sigma = 1$ and $2.51 \leq \epsilon \leq 4.27$. An example flow field is shown in Fig. 1 for $\epsilon = 4.27$. The dynamics of these patterns are quite complex making it very difficult to relate features of the flow field dynamics with the variation in the Lyapunov exponents. In this regime there are typically multiple roll pinch-off events occurring simultaneously.

In Fig. 5(a) we plot the spectrum of Lyapunov exponents λ_k for a convection domain where $\Gamma = 10, \sigma = 1, \epsilon = 2.51$. The dynamics is chaotic ($\lambda_1 > 0$) and the error bars represent the standard deviation of λ_k about its mean value at long times.

Figure 5(b) shows the zero-time cross-correlation between $\tilde{\lambda}_1$ and $\tilde{\lambda}_j$ where $j = 2, \ldots, N_\lambda$, we have first subtracted off the mean value of each of the Lyapunov exponents, and N_λ is the number of Lyapunov exponents computed for that value of ϵ. We find a positive cross-correlation for all of the exponents $\tilde{\lambda}_j$. The first several exponents have the largest cross-correlation with $\tilde{\lambda}_1$ which is then followed by a rather uniform fall-off with increasing j. These results suggest that all of the exponents tend to exhibit variations together. In these patterns the dynamics are dominated by roll pinch-off events suggesting that all of the exponents are sensitive to these events.

B. The Dynamics of the Leading Order Lyapunov Vector

The spatial and temporal dynamics of the leading order Lyapunov vector provides insight into regions of the flow field experiencing the largest growth in the perturbation equations. This has been used to identify non-repeating roll pinch-off events as significant contributors to the overall disorder in a chaotic convection flow field [13]. It has also been shown that Rayleigh-Bénard convection exhibits extensive chaos for finite cylindrical geometries using systems parameters that yield spiral defect chaos. For the parameters used by Paul *et al.*, $\epsilon = 2.51$ and $\sigma = 1$, the onset of extensivity occurred for a system size of $\Gamma \approx 7$ [14]. It is expected that extensive chaos occurs for convection layers that have reached a large-system limit where the influence of the lateral sidewalls have become reduced.

In order to explore this further we have performed very long-time numerical simulations for cylindrical geometries over a range of aspect ratios $5 \leq \Gamma \leq 30$ where $\epsilon = 2.51$ and $\sigma = 1$. In these simulations we have computed the leading-order Lyapunov exponent and Lyapunov vector. Figure 6 shows grey-scale contours of the

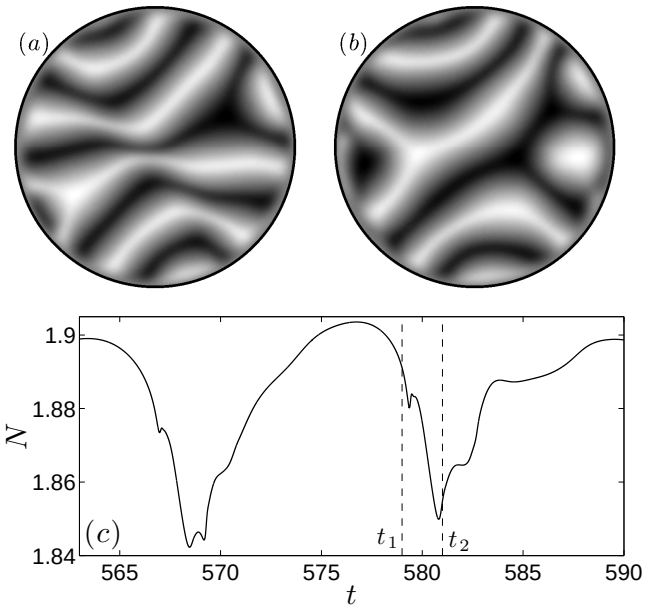

FIG. 3: The flow field and the variation of the Nusselt number N with time for periodic dynamics. The simulation parameters are $\Gamma = 5$, $\sigma = 1$, and $\epsilon = 1.93$. (a) The flow field at $t = 579$. (b) The flow field at $t = 581$. (c) The variation $N(t)$ for one period of the dynamics. The vertical lines represent the instances of time of the two flow field images.

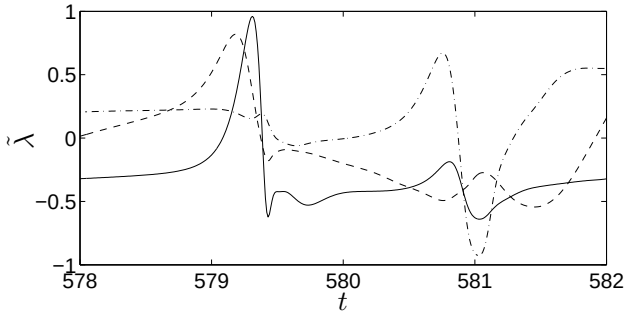

FIG. 4: The time variation of the first three instantaneous Lyapunov exponents $\tilde{\lambda}$ for time periodic dynamics. The simulation parameters are $\Gamma = 5$, $\sigma = 1$, and $\epsilon = 1.93$. The Lyapunov exponents have been normalized by the maximum value of λ_1 for ease of comparison. The values for $\tilde{\lambda}_1$, $\tilde{\lambda}_2$, and $\tilde{\lambda}_3$ are given by the solid, dashed, and dash-dot lines, respectively.

leading order Lyapunov vector overlaid with solid black lines indicating the convective roll pattern. The Lyapunov vector is plotted using the value of the thermal perturbation field at the horizontal mid-plane. In this figure light regions indicate large positive values, dark regions indicate large negative values, and grey regions represent regions of small growth. The images of Fig. 6 suggest that the smaller domains are dominated by large values of the perturbation at the lateral boundaries. This

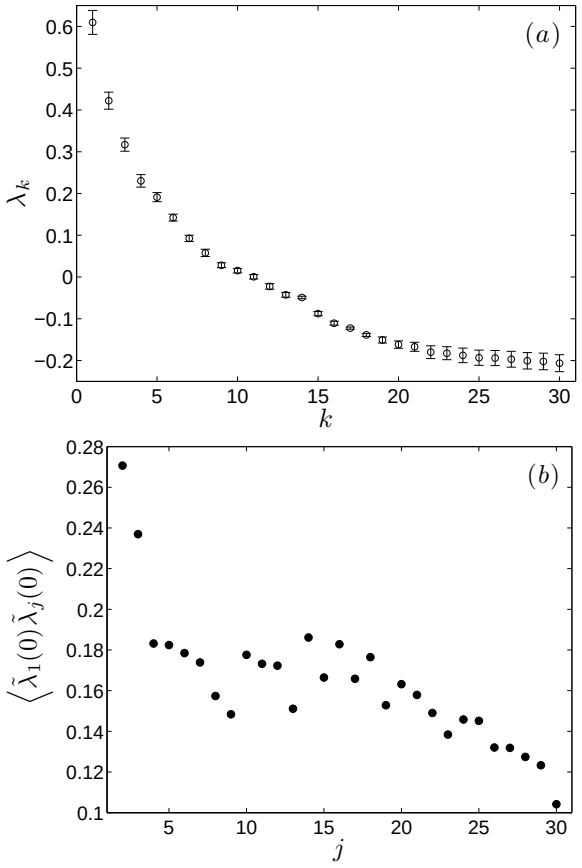

FIG. 5: (a) The spectrum of Lyapunov exponents λ_k. Also shown are the error bars that are computed from the standard deviation of λ_k about its mean value at long times. (b) The instantaneous cross-correlation between the leading order Lyapunov exponent and the remaining exponents in the spectra λ_j for $j = 2 \ldots 30$. The simulation parameters for both panels are $\sigma = 1$, $\Gamma = 10$, and $\epsilon = 2.51$.

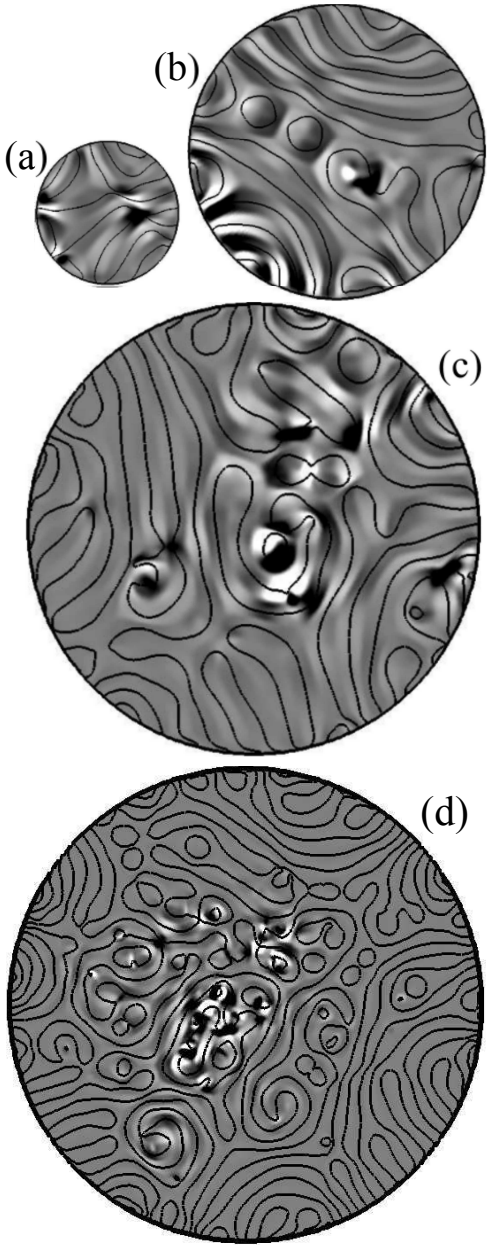

FIG. 6: Overlay of a grey-scale contours of the midplane temperature perturbation field with solid black lines representing the convection roll boundaries for different aspect ratios: (a) $\Gamma = 5$, (b) $\Gamma = 10$, (c) $\Gamma = 15$, and (d) $\Gamma = 30$. For $\Gamma = 30$ the image is plotted at half scale to be able to fit on this figure. The parameters are $\epsilon = 2.51$ and $\sigma = 1$.

transitions to dynamics with large perturbations in the bulk of the domain away from the sidewalls for the larger aspect ratio systems. The location of occurrence of the largest perturbations also shows a transition. In small domains, mostly bending rolls cause large perturbations; but in large domains, they are associated with the dislocation defects initiated by roll pinch-off events.

In order to investigate this further we have computed the time average of the magnitude of the leading order Lyapunov vector given by,

$$\langle \delta T(x,y) \rangle_t = \frac{1}{N_s} \sum_{i=1}^{N_s} |\delta T^{(1)}(x,y,z=0.5,t_i)|, \qquad (16)$$

where t_i is the time of the corresponding perturbation field, $N_s \approx 10^3$ is the total number of perturbation fields, and the notation $\langle \cdot \rangle_t$ is used to indicate the time-average. The spatial distribution of the time-averaged perturbation fields are shown in Fig. 7. In Fig. 7 red indicates regions of large values of the magnitude (located primarily near the boundary for small domains and at the bulk of the domain for large domains) and blue represents regions of small values of the magnitude (located mainly at the bulk of the domain for small domains and near the boundary for large domains). The asymmetry in the azimuthal direction of the averaged perturbation fields is most likely a result of the finite time of the simulations and the particular choice of random initial conditions. These simulations are quite computationally expensive

and we have not explored this aspect further. In order to explore the variation with the radial coordinate we have computed the azimuthal average of the time-averaged perturbation fields using,

$$\langle \delta T(\bar{r}) \rangle_{t,\theta} = \frac{1}{N_\theta} \sum_{i=1}^{N_\theta} \langle \delta T(\bar{r}, \theta) \rangle_t \,, \tag{17}$$

where the notation $\langle \cdot \rangle_{t,\theta}$ indicates time and azimuthal averaging, $\bar{r} = r/\Gamma$ is the normalized radial coordinate whose origin is in the center of the domain, and $N_\theta = 400$ is the number of points used in computing the azimuthal average. The radial variation of $\langle \delta T(\bar{r}) \rangle_{t,\theta}$ is plotted in Fig. 8. The transition from dynamics with significant perturbations at the boundaries to dynamics with significant perturbations away from the walls is evident.

C. The Variation of the Fractal Dimension with System Parameters

The variation of the fractal dimension with system parameters can provide insights into the nature and composition of the underlying high-dimensional attractor describing the chaotic dynamics. For Rayleigh-Bénard convection $D_\lambda = D_\lambda(\epsilon, \sigma, \Gamma)$. Our approach is to compute the variation of D_λ with one of the parameters while the remaining two are held constant. This has allowed us to quantitatively probe the underlying attractor for three different limiting cases. By increasing the system size while holding ϵ and σ constant we are able to quantify the increase in the fractal dimension in the spatiotemporal chaos limit [1]. When the driving ϵ is increased while holding Γ and σ constant we are able to quantify the increase in the fractal dimension with the addition of new degrees of freedom as the system approaches the strong driving limit. Lastly, the magnitude of the Prandtl number σ is inversely related to the magnitude of the mean flow. By the varying σ while holding Γ and ϵ constant we quantify the variation of the fractal dimension as the system transitions from non-potential to potential dynamics.

The variation of the fractal dimension with system size is expected to be extensive where

$$D_\lambda \propto \Gamma^{d_s} \tag{18}$$

in the large system limit and d_s is the number of spatially extended directions [30]. For Rayleigh-Bénard convection in large shallow layers $d_s = 2$. Extensive chaos has been demonstrated in large periodic convection layers [11] and in finite cylindrical convection layers [14]. Deviations from extensive chaos for small changes in system size has been proposed as a means to identify a length scale associated with the fundamental structures composing spatiotemporal chaos [31]. Deviations from extensivity have been found using the complex Ginzburg-Landau equation [31], the Lorenz-96 equations [32] and systems of coupled map lattices [33]. However, microextensivity has been found for the Kuramoto-Sivashinsky equation [34]. For Rayleigh-Bénard convection we have found that the slow and noisy convergence of D_λ (see Fig. 2) precludes such an investigation using currently available algorithms and computing resources.

The variation of D_λ with ϵ and σ is shown in Fig. 9. Fig. 9(a) illustrates the variation of D_λ with ϵ where $\sigma = 1$ and $\Gamma = 10$. A typical flow field pattern for the largest value of the forcing $\epsilon = 4.27$ is shown in Fig. 1. The error bars represent the standard deviation of D_λ about its mean value in the large-time limit. The solid line through the data is a curve fit given by

$$D_\lambda = \alpha \epsilon^4 + \beta \tag{19}$$

where $\alpha = 0.095$ and $\beta = 19.4$. This relationship is only useful for $\epsilon \gtrsim 2.5$. For smaller value of ϵ there must be a transition not captured in our data that would yield a vanishing value of the fractal dimension at some positive and finite value of ϵ. It is possible that our curve fit remains valid for Rayleigh numbers larger than what is shown, however without further evidence this remains speculative. It is interesting to note that Sirovich and Deane [35] found that the fractal dimension increases linearly with Rayleigh number from numerical simulations of turbulent Rayleigh-Bénard convection ($\epsilon \approx 70$) in a small periodic box with free-slip boundaries.

The fractal dimension can be used to provide an estimate for a natural chaotic length scale [1],

$$\xi_\delta \equiv \left(\frac{D_\lambda}{\Gamma^{d_s}} \right)^{-1/d_s} \tag{20}$$

where a volume of size $\xi_\delta^{d_s}$ contains a single chaotic degree of freedom on average. The variation of ξ_δ with ϵ is shown in Fig. 10 where it decreases from approximately 2 to 1.5 over the range of ϵ explored. In order to compare this with features of the spatial patterns we have computed the time averaged value of the pattern wavelength ξ_L from the structure factor [1]. The pattern wavelength increases from approximately 3 to 4 over the range explored. The ratio ξ_L/ξ_δ provides an estimate for the number of chaotic degrees of freedom per wavelength of the flow field pattern and is also shown on Fig. 10. This indicates that the number of chaotic degrees of freedom per wavelength of the pattern is increasing with increasing ϵ. This is reflected by the occurrence of smaller scale features in the pattern images.

The variation of the fractal dimension with Prandtl number is shown in Fig. 9(b). The corresponding images of the flow field patterns are shown in Fig. 11. As the Prandtl number increases the magnitude of the mean flow decreases and eventually the spiral defect chaos state vanishes and is replaced with a stationary pattern [17]. We find that the fractal dimension decreases rapidly with increasing σ as shown by the solid line in Fig. 9(b). For the range $1 \leqslant \sigma \lesssim 2$ the solid line is a curve fit given by

$$D_\lambda = \alpha \sigma^{-\beta} - \gamma \tag{21}$$

where $\alpha = 44.95$, $\beta = 1.06$ and $\gamma = 20.91$. This curve fit was determined using numerical results in the range $1 \leqslant \sigma \leqslant 1.8$ and it predicts the zero of the fractal dimension to occur at $\sigma = 2.06$. From our numerical results the fractal dimension vanishes to within the accuracy of our calculations for $\sigma \geqslant 2$ and is represented by the horizontal solid line. For $\sigma \geqslant 2$ the fluid patterns slowly evolve to a time-independent stationary pattern as shown in Fig. 11(b)-(d). Our results suggest that the fractal dimension is inversely proportional to the Prandtl number. It is interesting to point out that this is similar to the variation of the mean flow magnitude with the Prandtl number as discussed by Chiam *et al.* [17].

IV. CONCLUSIONS

A fundamental understanding of high-dimensional chaotic dynamics in spatially extended systems remains a vast and important challenge. In this paper, we have used large scale numerics to provide a quantitative link between powerful ideas of dynamical systems theory and a fluid system that can be explored in the laboratory. We have gone to considerable computational effort to perform simulations for the geometries, boundary conditions, and system parameters that are of experimental relevance. Our computation of the Lyapunov based diagnostics provide results that are currently not possible to obtain analytically or experimentally and we have used these to provide new physical insights. Although the Lyapunov based diagnostics we have quantified are not directly accessible to experimental measurement, at least not in any straightforward way that we can suggest, the values we present are an important benchmark for comparison as further experimental and theoretical work is conducted. For example, it may be possible to connect our results with experimental measurements using ideas based upon Lagrangian coherent structures [36, 37] or computational homology [38]. From a theoretical point of view, our work suggests that it would be interesting to explore the dynamics of the spectrum of Lyapunov *vectors* using the more recently suggested approach of characteristic Lyapunov vectors that satisfy Oseledec splitting [39, 40]. Overall, we anticipate that our results will be useful to those interested in controlling, predicting, and modeling high-dimensional chaotic systems.

Acknowledgments: The computations were conducted using the resources of the Advanced Research Computing center at Virginia Tech and the research was supported by NSF grant no. CBET-0747727. We have also had many fruitful discussions with Mike Cross, Paul Fischer, Janet Scheel, Keng-Hwee Chiam, Magnus Einarsson, and Nicholar O'Connor.

[1] M. C. Cross and P. C. Hohenberg, Rev. of Mod. Phys. **65**, 851 (1993).
[2] E. N. Lorenz, J. Atmos. Sci **20**, 130 (1963).
[3] P. Holmes, J. L. Lumley, and G. Berkooz, *Turbulence, coherent structures, dynamical systems, and symmetry* (Cambridge University Press, Cambridge, UK, 1996).
[4] C. R. Nugent, W. M. Quarles, and T. H. Solomon, Phys. Rev. Lett. **93**, 218301 (2004).
[5] M. Bar and M. Eiswirth, Phys. Rev. E **48**, R1635 (1993).
[6] H. D. I. Abarbanel, *Analysis of Observed Chaotic Data* (Springer, 1996).
[7] J. D. Farmer, E. Ott, and J. A. Yorke, Physica D **7**, 153 (1983).
[8] A. Wolf, J. B. Swift, H. L. Swinney, and J. A. Vastano, Physica D **16**, 285 (1985).
[9] E. Ott, *Chaos in dynamical systems* (Cambridge University Press, New York, 1993).
[10] E. Bodenschatz, W. Pesch, and G. Ahlers, Annu. Rev. Fluid Mech. **32**, 709 (2000).
[11] D. A. Egolf, I. V. Melnikov, W. Pesch, and R. E. Ecke, Nature **404**, 733 (2000).
[12] S. W. Morris, E. Bodenschatz, D. S. Cannell, and G. Ahlers, Phys. Rev. Lett. **71**, 2026 (1993).
[13] J. D. Scheel and M. C. Cross, Phys. Rev. E **74**, 066301 (2006).
[14] M. R. Paul, M. I. Einarsson, P. F. Fischer, and M. C. Cross, Phys. Rev. E **75**, 045203 (2007).
[15] A. Jayaraman, J. D. Scheel, H. S. Greenside, and P. F. Fischer, Phys. Rev. E **74**, 016209 (2006).
[16] G. Ahlers, S. Grossmann, and D. Lohse, Rev. Mod. Phys. **81**, 503 (2009).
[17] K.-H. Chiam, M. R. Paul, M. C. Cross, and H. S. Greenside, Phys. Rev. E **67**, 056206 (2003).
[18] H. S. Greenside, M. C. Cross, and W. M. Coughran Jr., Phys. Rev. Lett. **60**, 2269 (1988).
[19] V. Croquette, P. Le Gal, and A. Pocheau, Phys. Scr. **T13**, 135 (1986).
[20] A. Pocheau, V. Croquette, P. Le Gal, and C. Poitou, Europhys. Lett. **3**, 915 (1987).
[21] A. C. Newell, T. Passot, and M. Souli, Phys. Rev. Lett. **64**, 2378 (1990).
[22] A. C. Newell, T. Passot, and M. Souli, J. Fluid Mech. **220**, 187 (1990).
[23] M. C. Cross and A. C. Newell, Physica D **10**, 299 (1984).
[24] G. Ahlers, Phys. Rev. Lett. **33**, 1185 (1974).
[25] M. R. Paul, M. C. Cross, P. F. Fischer, and H. S. Greenside, Phys. Rev. Lett. **87**, 154501 (2001).
[26] M. R. Paul, K.-H. Chiam, M. C. Cross, P. F. Fischer, and H. S. Greenside, Physica D **184**, 114 (2003).
[27] A. Duggleby and M. R. Paul, Computers and Fluids **39**, 1704 (2010).
[28] P. F. Fischer and A. T. Patera, Annu. Rev. Fluid Mech. **26**, 483 (1994).
[29] P. F. Fischer, J. Comp. Phys. **133**, 84 (1997).
[30] D. Ruelle, Commun. Math. Phys. **87**, 287 (1982).
[31] M. P. Fishman and D. A. Egolf, Phys. Rev. Lett. **96**, 054103 (2006).
[32] A. Karimi and M. R. Paul, Chaos **20**, 043105 (2010).
[33] C. S. O'Hern, D. A. Egolf, and H. S. Greenside, Phys. Rev. E **53**, 3374 (1996).

[34] S. Tajima and H. S. Greenside, Phys. Rev. E **66**, 017205 (2002).
[35] L. Sirovich and A. E. Deane, J. Fluid Mech. **222**, 251 (1991).
[36] G. A. Voth, G. Haller, and J. Gollub, Phys. Rev. Lett. **88**, 254501 (2002).
[37] G. Haller, Physica D **149**, 248 (2001).
[38] H. Kurtuldu, K. Mischaikow, and M. Schatz, Phys. Rev. Lett. **107**, 034503 (2011).
[39] F. Ginelli, P. Poggi, A. Turchi, H. Chatè, R. Livi, and A. Politi, Phys. Rev. Lett. **99**, 130601 (2007).
[40] D. Pazó, I. G. Szendro, J. M. López, and M. A. Rodríguez, Phys. Rev. E **78**, 016209 (2008).

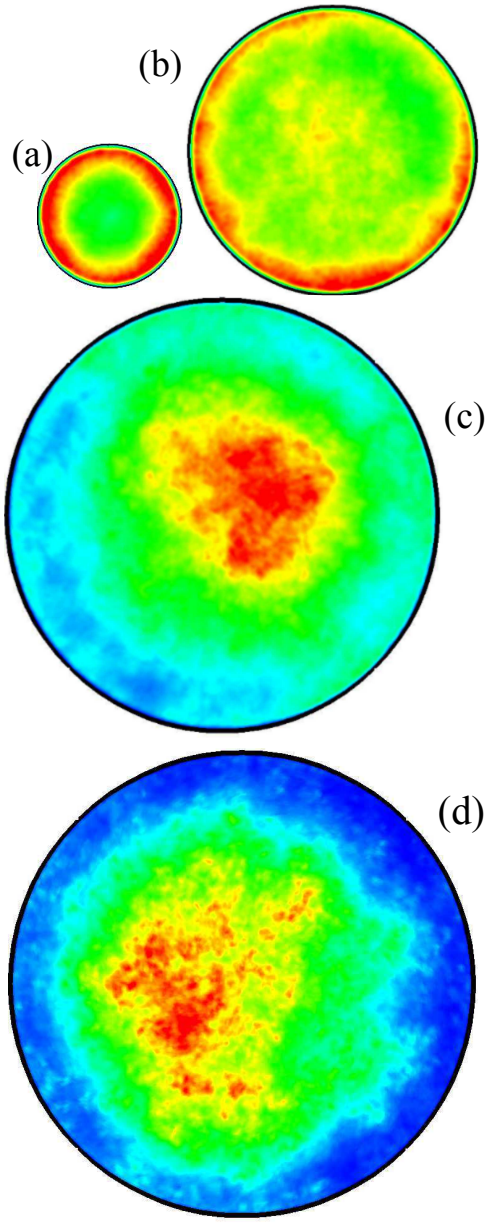

FIG. 7: (Color online) The spatial variation of the time-averaged magnitude of the thermal perturbation field $\langle \delta T(x,y) \rangle_t$ evaluated at the horizontal mid-plane. (a) $\Gamma = 5$, (b) $\Gamma = 10$, (c) $\Gamma = 15$, and (d) $\Gamma = 30$. The simulation parameters are $\epsilon = 2.51$ and $\sigma = 1$. The image for $\Gamma = 30$ is plotted at half scale to fit on this figure. In the color contour, red regions (located primarily near the boundary for small Γ and at the bulk of the domain for large Γ) correspond to the large magnitude of the perturbation and blue regions (located mainly at the bulk of the domain for small Γ and near the boundary for large Γ) associate with the small magnitude of the perturbation.

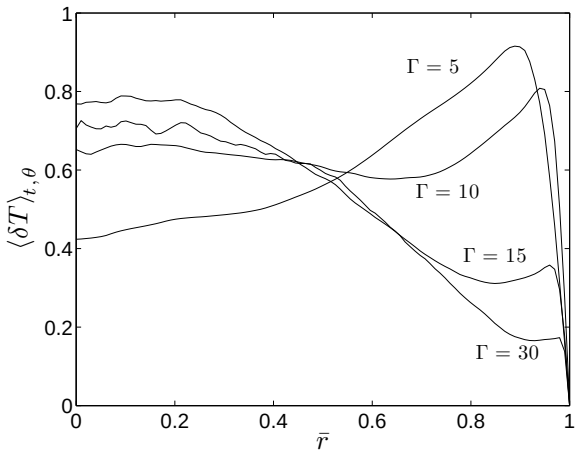

FIG. 8: The radial variation of the azimuthal and time averaged thermal perturbation field $\langle \delta T(\bar{r}) \rangle_{t,\theta}$. The aspect ratios are $5 \leq \Gamma \leq 30$.

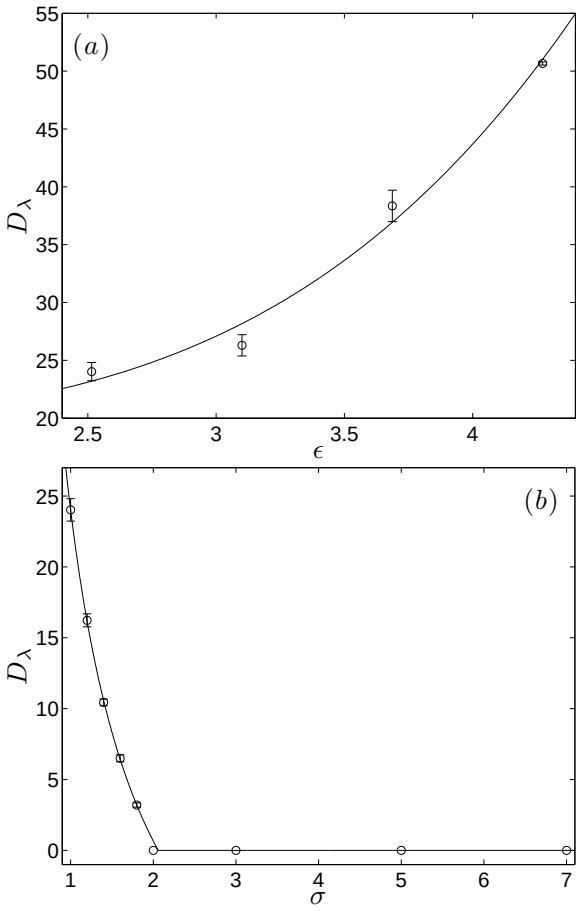

FIG. 9: (a) The variation of the fractal dimension with Rayleigh number for $\Gamma = 10$ and $\sigma = 1$. The circles are data points from the simulations and the solid line is the curve fit $D_\lambda = 0.095\epsilon^4 + 19.4$. (b) The variation of the fractal dimension with Prandtl number for $\Gamma = 10$ and $\epsilon = 2.51$. The circles are data points from the simulations and the solid line is a power-law curve fit as $D_\lambda = 44.95\sigma^{-1.06} - 20.91$ for $1 \leqslant \sigma < 2$ and $D_\lambda = 0$ for $\sigma \geqslant 2$.

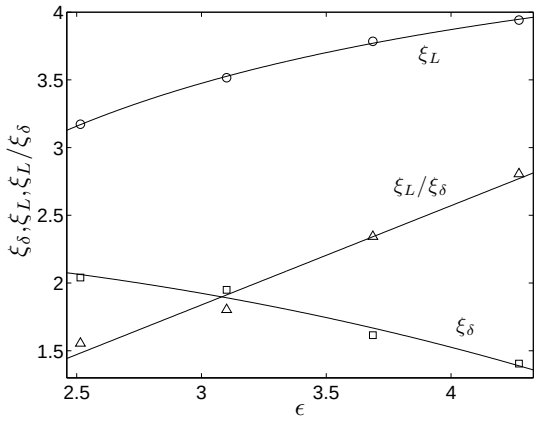

FIG. 10: The variation of the natural chaotic length scale (ξ_δ), the wavelength of the pattern (ξ_L), and the ratio of ξ_L/ξ_δ with ϵ for $\Gamma = 10$ and $\sigma = 1$. The open squares show ξ_δ, the open circles show ξ_L, the open triangles demonstrate ξ_L/ξ_δ, and the solid lines illustrate curve fits for ξ_δ and ξ_L as $\xi_\delta = 2.32 - 0.03\epsilon^{2.4}$ and $\xi_L = 5.07 - 4.75\epsilon^{-0.99}$ and linear fit for the ratio as $\xi_L/\xi_\delta = 0.73\epsilon - 0.36$.

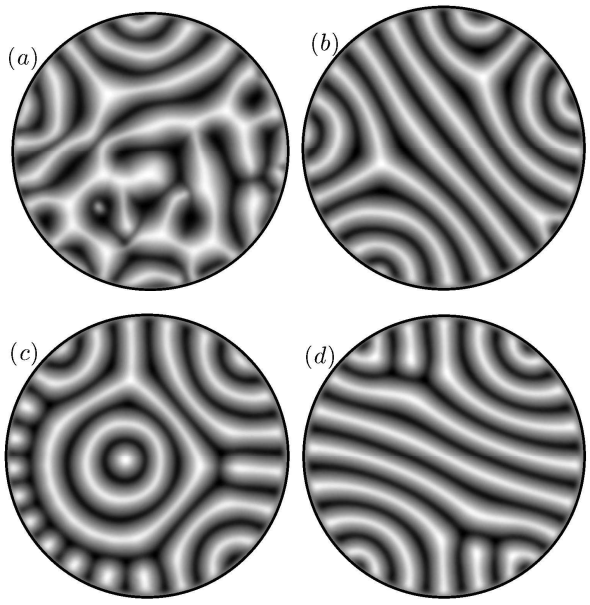

FIG. 11: The flow field patterns for different Prandtl numbers. In each case $\epsilon = 2.51$ and $\Gamma = 10$. Panel (a) $\sigma = 1$, (b) $\sigma = 3$, (c) $\sigma = 5$, (d) $\sigma = 7$.